Astron. Astrophys. 362, 342–358 (2000)

ASTRONOMY AND ASTROPHYSICS

Alfvén wave propagation in the high solar corona

R. Grappin, J. Léorat, and A. Buttighoffer

DAEC, Observatoire de Paris, Université Paris VII, CNRS (UMR 8631), 92195 Meudon Cedex, France
and ASCI, 91400 Orsay, France

Received 8 June 2000 / Accepted 25 August 2000

Abstract. We consider monochromatic Alfvén perturbations propagating upward in the high corona, in the distance range between 2 and 9 solar radii. The corona is made of a closed loop region and of an open flow region, with or without structured streams generated by stationary temperature inhomogeneities in the corona. The wave period is 36 min., the plasma β varies between 0.25 at the poles and 1.2 at the equator. We integrate the time-dependent, three-dimensional axisymmetric polytropic MHD equations. Filters are used to damp energy at the grid scale. The mean flow and waves are dealt with self-consistently, by using transparent boundary conditions, which prevent spurious reflections at the inner coronal boundary.

We find that the mother Alfvén wave remains everywhere Alfvénic: the normalized cross-helicity is $\sigma_c \simeq 1$–10^{-3} except within a thin layer around the heliospheric current sheet. The radial evolution depends on the latitude. In a large domain around the heliospheric current sheet, the wave is very strongly damped, whatever its amplitude, by the phase mixing, i.e., the shear of the wave front due to transverse gradients of the Alfvén speed and bulk velocity. As a consequence, the Alfvén wave nowhere reaches the heliospheric current sheet. At higher latitudes, and outside structured streams, the amplitude varies in agreement with the WKB prediction, albeit with some dissipation due to nonlinear steepening (depending on the wave amplitude); as a rule, the propagation angle varies, i.e., the propagation is alternatively oblique and quasi-parallel. On the other hand, streams show specific properties: the amplitude does not follow the WKB law, but the propagation angle remains constantly oblique. As a consequence, the streams show a strong minimum in the amplitude of the compressive fluctuations.

Key words: Magnetohydrodynamics (MHD) – waves – methods: numerical – Sun: corona – Sun: solar wind

1. Introduction

The solar wind plasma considered, say, in the distance range from two solar radii up to 100 solar radii, is highly inhomogeneous. It shows large-scale systematic gradients, both in the radial and transverse directions, the heliospheric current sheet (HCS) providing a kind of symmetry surface. It is also highly turbulent in the domain explored in situ: the spectrum of fluctuations extends over several frequency decades, starting from the heliospheric distance scale. A part of the fluctuating energy is made of Alfvén, or Alfvén-like waves; another part is made of quasi-static, pressure-balanced structures convected by the wind. Remarquable examples of such structures are provided by the so-called channels observed by Buttighoffer et al. (1995, 1999).

The properties of waves may be summarized as follows (e.g., Marsch, 1991). Far enough from the current sheet: upward propagating Alfvén waves are identified clearly via a maximal normalized cross-helicity (see definition below, Eq. 10); their radial evolution follows the WKB prediction, but for some damping; the modulus of the magnetic field vector is close to constant, i.e., the tip of the vector shows a random walk on a sphere (spherical Alfvén waves, see Vasquez & Hollweg, 1998). Close to the current sheet, fluctuations are still present, but the signature of Alfvén waves is lost, i.e., the cross-helicity is close to zero, and compressive fluctuations are more important.

Because the cross-helicity is maximal (or nearly so) far from the HCS, the waves should be mainly propagating in one direction, so that the problem of the formation and evolution of the wave spectrum differs from the classical problem of turbulence, in which both species of Alfvén waves couple (e.g., Grappin & Mangeney, 1996). The theoretical understanding of the problem of unidirectional Alfvén wave propagation in the solar wind may be summarized as follows. (i) The WKB analysis allows to relate, for small amplitude and high frequency waves, the radial evolution of the amplitude to that of the plasma parameters (Alfvén speed and bulk velocity). It has been mostly applied to radial winds with radial magnetic fields (see however Usmanov et al., 2000). (ii) The nonlinear evolution of the Alfvén waves involves the coupling with the compressive modes, which depends on the angle of propagation with respect to the mean field. A parallel propagating Alfvén wave forces an acoustic wave via its ponderomotive force, while an oblique propagating wave forces a fast wave propagating also at the Alfvén wave speed, and which has the property of minimizing the variation of the magnetic field pressure, thus leading to an arc wave, and eventually to a rotational discontinuity (Barnes & Hollweg, 1974; Vasquez & Hollweg, 1998). (iii) The large scale gradient of the

Send offprint requests to: R. Grappin (Roland.Grappin@obspm.fr)

magnetic fluctuating energy leads, to second order, to an additional contribution to the thermal pressure gradient: this additional pressure has been proposed as a mean to accelerate the fast solar wind (Alazraki & Couturier, 1971).

The oblique propagation scenario seems to fit well the observations, but it has never been verified that it works in a self-consistent numerical model of such a highly inhomogeneous plasma as the solar wind. This point is important, as the evolution, and in particular the damping of the Alfvén wave, depends on the degree of magnetic pressure imbalance, which induces in turn magnetosonic waves which are subjected to moderate or strong damping, depending on the plasma β (Barnes, 1966).

Our aim here is to analyse the Alfvén wave propagation properties in a simulated solar wind which shares some of the properties characterizing the real solar wind, namely the radial stratification and transverse structures. Our approach is to integrate the axisymmetric MHD equations with polytropic index equal to unity. This choice of $\gamma = 1$ is a zero-order model for the complex kinetic heating phenomena which lead to the low average radial temperature gradient in the corona. On the other hand, we take fully into account the nonlinear coupling between waves and the wind. This is to our knowledge the first self-consistent simulation of the nonlinear wave-wind interaction in the context of an MHD wind with both open and closed field lines. A preliminary account of the present work has been presented at the Soho 8 workshop (Grappin et al. 1999).

There are two steps in studying the wave-wind interaction. First, we have to establish a (stable) stationary wind, then we must perturb it. Note that the position of the boundaries of the numerical domain is important. Indeed, most of the solutions found in domains not including the sonic and Alfvénic surfaces are artificial, because the absence of the sonic surface leads to a too large number of freedoms in the numerical experiment. In reality, the sonic surface acts as a filter which imposes relations between the different fields, in particular between temperature and velocity. Thus we include the accelerating region in the numerical domain (Grappin et al. 1997a and b; Grappin & Léorat 1998).

To generate the wind, we start with a static atmosphere and an external magnetic dipole, and perturb the atmosphere with a pressure disturbance. The perturbation leads to a global flow which generates an induced magnetic field comparable to the external field, resulting in the opening of most field lines, except around the equator. The atmosphere finally adopts after some time (a few days) a new equilibrium state, made of a transonic Parker-like wind at high latitudes, and of a helmet streamer at low latitudes, i.e., a stagnant region with a slow wind on the top of it. The plasma β is larger than unity in the stagnant region, and smaller than unity in the open flow region, except at large distances. More specifically, β at the inner boundary is about 1.2 at the equator, and 0.25 at the poles. The whole wind is slow compared to the real wind, i.e., its maximum (i.e., polar) speed at 9 solar radii is not larger than $300\,\mathrm{km\,s^{-1}}$, taking a coronal temperature $T = 1.310^6$ K. Such a solution is similar to other previously obtained stationary solutions (Pneuman & Kopp 1971; Washimi et al. 1987; Linker & Van Hoven 1990; Wang et al. 1993).

Because we are interested in the role played by advected stationary structures, we also consider a wind with imbedded pressure-balanced structures (see below Fig. 1). These pressure-balanced structures are generated by two regions at the inner boundary which are maintained at a temperature lower than average. Note that in the subsonic region, decreasing locally the inner boundary temperature is the only way we know to generate collimated persistent structures; in particular, imposing a low velocity at the inner boundary without decreasing the temperature does not lead to a persistent slow stream because of the attraction of the local transonic solution (Grappin et al. 1997a).

In order to study wave propagation, we must introduce perturbations into the medium. This is done by controling the incoming characteristics at the subsonic boundary (the inner boundary). This has already been done with success in a non magnetic wind (Grappin et al., 1997b) and in a magnetic, plane-parallel atmosphere (Velli et al., 1997). The case of an MHD wind (with curved geometry) proves to be unstable when we want to control waves entering the domain but want the fluctuations to propagate freely outward. These numerical instabilities are cured here by a careful adaptation of the spatial schemes (derivatives and filtering), and by coupling the perturbed wind with the unperturbed wind. The numerical experiment thus has two successive phases: during the first phase, the stationary wind is established as described above, using boundary conditions which are stable but do not allow to inject waves; during the second phase, we control the wave injection, and couple (weakly) the boundary solution with the stationary wind solution in order to stabilize the system (Eq. (7) below).

A related problem has been considered by Ofman & Davila (1998) who inject Alfvén waves at the basis of an axisymmetric region around a pole, with a transverse density gradient, and all field lines open. The authors control directly the field amplitude at the coronal base, which ensures stability but in general leads to reflective boundaries; in the open field geometry studied by the authors, this is of no consequence because no waves propagate backward to the coronal boundary. In the present work where a whole meridian including closed and open field lines is considered, we must use a fully non-reflecting scheme, otherwise the waves propagating along closed lines would be reflected artificially by the boundaries.

The plan of the paper is as follows. Sect. 2 explains the method followed to inject the waves at the inner boundary. Sect. 3 contains the results, Sect. 4 the discussion, and Sect. 5 the conclusion.

2. Method

2.1. Equations and numerical scheme

We integrate the MHD equations in spherical coordinates r, θ, ϕ for the pressure P, the velocity u, magnetic field B, density ρ and temperature T. No longitude dependance is considered (axisymmetric condition). The equations read:

$$\frac{\partial \rho}{\partial t} + div(\rho \mathbf{u}) = 0$$

$$\frac{\partial \mathbf{u}}{\partial t} + (\mathbf{u}.\nabla)\mathbf{u} = -\frac{\nabla P}{\rho} + \frac{1}{\mu_0 \rho}(\mathbf{curl B} \times \mathbf{B}) - \frac{GM}{r^2} + \nu \Delta \mathbf{u}$$

$$\frac{\partial \mathbf{B}}{\partial t} = \mathbf{curl}(\mathbf{u} \times \mathbf{B}) + \eta \Delta \mathbf{B} \quad (1)$$

$$\frac{\partial T}{\partial t} + (\mathbf{u}.\nabla)T = (1-\gamma) T div \mathbf{u}$$

$$P = 2\rho k T/m$$

M is the solar mass; in the last equation, k is Boltzman constant, and m is the proton mass. The polytropic index is taken unity, which implies that temperature inhomogeneities are advected without change.

The magnetic field B is the sum of a given, external dipolar field B^0 and of the field induced by the flow. In order to satisfy the divergence-free condition, we do not solve directly the equations above for the meridional magnetic field (i.e., components B_r and B_θ). We consider sucessively the interior of the domain and its outer (supersonic) boundary, and then the inner (subsonic) boundary. Inside the domain, we solve the equation for the magnetic potential ψ:

$$\partial \psi / \partial t = u_r B_\theta - B_r u_\theta \quad (2)$$

and then derive the r and θ components of the magnetic field by using:

$$\mathbf{B} = \mathbf{rot}(\psi \mathbf{e}_\phi) + B_\phi \mathbf{e}_\phi + \mathbf{B}^0 \quad (3)$$

that is

$$B_r = B_r^0 + \frac{1}{r}(\psi \cot\theta + \partial\psi/\partial\theta) \quad (4)$$

$$B_\theta = B_\theta^0 - \frac{\psi}{r} - \partial\psi/\partial r \quad (5)$$

The form of the equations changes at the inner boundary, where the boundary conditions are imposed using the characteristic form of the equations, as explained below. In particular, we do not integrate directly the equation for the magnetic potential (which cannot be put in characteristic form), but instead we first solve the equation for B_θ in terms of characteristics, and then inverse (integrate) equ. 5 to obtain the boundary value of the potential (Velli et al., 1997). Let us write formally this solution for the magnetic potential at the boundary as:

$$\partial \psi / \partial t = H(\partial B_\theta / \partial t) \quad (6)$$

The preceding equation works well during the first phase, during which the stationary wind solution is obtained, because during this phase we do not attempt to inject perturbations, and thus use incomplete control of the incoming characteristics (see below). Let us call ψ^0 the magnetic potential at the inner boundary which is obtained at the end of this first phase. During the second phase, the injection of waves forces to adopt a full control of the incoming characteristics, which makes the boundaries unstable. To stabilize the system, we couple the magnetic potential ψ with the unperturbed magnetic potential ψ^0 obtained during the first phase. This coupling appears in the equation which allows to derive the magnetic potential from the poloidal magnetic field as:

$$\partial \psi / \partial t = H(\partial B_\theta / \partial t) - (\psi - \psi^0)/\tau \quad (7)$$

where the coupling time τ is about 8.4 hours, a time lapse much longer than the period of the waves we are interested in, about 36 minutes: in this way, we expect that the effect of the coupling on both the wave injection will be negligible, and that the boundary will remain non-reflecting.

Table 1. Parameters of the numerical algorithms. Mesh denotes the grid point in the radial direction. r-Filter denotes the filter in the radial direction, etc... ψ denotes the algorithm used to compute the magnetic potential at the boundary from equ. 5. In each pair of numbers, the first (α) denotes the weigth given to non-diagonal terms in the implicit (tridiagonal) schemes of Lele (1992), and the second (n) denotes the order of the scheme.

Mesh	r-Filter	θ-Filter	$\partial/\partial r$	$\partial/\partial\theta$	ψ
1	none	0, 4	2, 3	1/3, 6	2, 3
2	0, 3	0, 4	1/4, 4	1/3, 6	none
> 2	0.475, 4	0, 4	1/3, 6	1/3, 6	none

A last question we must consider is that of the dissipative terms. There are two such terms appearing in the MHD equations: a viscous and a resistive term (and eventually also a thermal conduction term). Once the resolution has been chosen, the viscosity and resistivity have to be adapted so that grid scale fluctuations are correctly damped. In practice, at the moderate resolution used here (128 radial mesh points, 256 points in latitude), this leads to a much too fast damping of the largest scales. This problem is solved by replacing the Laplacians by implicit filters (Lele 1992) which minimize the dissipation of large scale fluctuations but still dissipate mesh size fluctuations generated by nonlinear coupling. Note that such a filtering method is not more, but not less realistic than molecular dissipation, since the solar wind plasma is actually a collisionless plasma in which the dissipation processes are far more complex than the ones valid for a collisional plasma.

We use spherical coordinates and finite differences, with a uniform grid in both coordinates. The temporal scheme is third order Runge-Kutta. Spatial derivatives and filters are computed by finite differences, solving implicit (or compact) algorithms given by Lele (1992). These implicit algorithms have the properties to have a very low error, compared to explicit algorithms of the same order. However, explicit algorithms for the derivatives are more stable. A careful adjustment of the order n and of the degree of impliciteness (parameter α, see Table 1) has been necessary to achieve stability of the boundaries. In the case of filters, note that the parameter α corresponds also to the strength of the filter: $\alpha = 0$ (explicit filter) corresponds to a much stronger filter than a non-zero α (implicit filter, see Lele (1992)).

2.2. Domain of integration and physical parameters

The numerical domain is a spherical shell between 1.8 and 8.9 solar radii. It has been chosen in order to have the flow subsonic and subalfvénic at the inner boundary and on the other hand supersonic and superalfvénic at the external boundary. (This being true except within the largest cold stream, which is slightly subalfvénic at the outer boundary). Hence, except within the largest cold stream, no information can propagate downward on the side of the outer boundary, so that no boundary condition is imposed at the outer boundary. At the inner boundary on the contrary, the flow is subsonic and subalfvénic everywhere, so that information must be provided concerning all upward propagating modes.

The temperature profile at the inner boundary is imposed via pressure-balanced fluctuations (or entropy characteristics). The coronal temperature is 1.310^6 K, corresponding to a sound speed of 160 km s^{-1}. The inhomogeneous runs (see Table 2) have two cold regions, with a 25% temperature drop (i.e., a temperature about 10^6 K), with angular size of respectively 5 and 10 degrees, the largest region being in the northern hemisphere.

In contrast to the temperature, the magnetic field at the inner boundary cannot be imposed, as this would imply reflecting boundaries. The only thing which can be imposed is the initial field, i.e., the external dipole field; the final equilibrium magnetic field is the sum of this initial field and of the field induced by the flow. At equilibrium, the r.h.s. of the induction equation is zero, which, except along the helmet streamer boundary where dissipation is substantial, is achieved by the plasma by having parallel velocity and magnetic fields. Note that the final intensity of the magnetic field depends entirely on the details of the transient phase. In the present case, the induced field is globally in the same direction as the external initial field, so that the final total field is larger, but this is not a rule: the final total field is lower than the external field in Grappin & Léorat (1998).

Here the initial Alfvén speed has its maximum amplitude at the pole of the inner boundary: it is 210 km s^{-1}. The final Alfvén speed at the polar boundary reaches 418 km s^{-1}. The final β of the plasma is 0.25 at the poles and 1.2 at the equator.

The incident Alfvén wave flux is fixed as explained below. The list of runs is given in Table 2. Runs are characterized by: the amplitude of the perturbation ϵ, the spatial extent of the perturbation (meridian or half-meridian, see the function $A^0(\theta)$ below), the presence of cold regions at the coronal level, the strength of the filter acting on the radial component of the velocity. The two main runs studied here are runs A and C, which will be compared in order to understand the effects related to the presence of cold streams; other runs will be useful to investigate specific points.

2.3. Inner boundary conditions: Phases 1 and 2

To fix the inner (subsonic) boundary conditions, we use the method of characteristics, which has been adapted to the MHD equations by (Hu & Wu 1984, Brio & Wu 1988, Vanajakshi et al. 1989). This method is actually the only way to take into account the time-dependent MHD equations at the boundary. It allows either to impose directly fields, or gradients, or, as we want to do here, to control perturbations entering the domain by the subsonic boundary, and at the same time let outgoing perturbations escape freely from the domain.

Table 2. List of runs. ϵ is the relative wave amplitude. The Latitude parameter is 1 if perturbation is applied on the whole hemisphere except the poles, 1/2 if applied on a half hemisphere. Mode denotes the injection mode: Su means that u_ϕ has a shear at the equator as in Eq. (12); Sb means that B_ϕ has a shear at the equator (no s parameter in Eq. (12)); both have $|B_\phi|/B$ independent of latitude; Su' is as Su, but the amplitude of u_ϕ is independent of latitude, (instead of that of $|B_\phi|/B$). Streams is the number of cold coronal regions. Filtering denotes the relative strength of the radial filter applied to u_r (strong corresponds to α =0, see Table 1).

Run	ϵ	Latitude	Mode	Streams	Filtering
A	0.14	1	Su	0	strong
B	0.14	1	Sb	0	strong
C	0.14	1	Su	2	weak
D	0.05	1	Su'	2	weak
E	0.14	1/2	Su	0	strong

Note that it is necessary to work with transparent boundaries because we consider the high corona; if we were to consider the inner boundary being at the photosphere, then it would be physically sound to control the velocity field in place of the incident wave flux (Demoulin, private communication). Also, if we were certain that there will be no subsonic perturbations propagating outward from the domain (i.e., downward), then it would be safe to use a simpler method in which we impose directly field fluctuations compatible with an upward propagation, as for instance in Ofman & Davila, (1998).

The control of wave injection requires, as mentioned in the introduction, some care. Indeed, we have found that instabilities at the boundaries appear when one wants at the same time a full control of the incoming perturbations, and boundaries transparent to outgoing perturbations. The decrease of the stability of the system at the boundary, compared to other problems (in hydrodynamics or plane-parallel atmospheres) seems to come from the fact that the expression of the characteristic terms which are necessary to obtain full control of the incoming perturbations only leads to redistributing transverse gradients of all fields in the evolution equation.

To stabilize the system, there are several solutions, which either amount to abandon full control of the flux of incoming perturbations (see Grappin & Leorat 1999), or to decrease the degree of transparency of the boundaries to outgoing perturbations. A first (common) way, used in previous works, is to impose the radial component of the magnetic field (by setting to zero the potential ψ at the boundary). This precludes full transparency, as any imposed field at the boundary interferes with outcoming waves and thus leads to reflections. Another method, which we use here, amounts to couple (as weakly as possible) a field with a given, reference field. This method is used for instance in two-dimensional hydrodynamical simula-

tions of open flows to prevent systematic drifts of the density at the inlet (Poinsot & Lele, 1993). In the present case, coupling with a density field is not useful: only coupling with the magnetic potential ψ helps in stabilizing the boundaries.

The computation is thus done in two phases. During the first phase, we compute the equilibrium wind. This is done by imposing partial control of the characteristics, with expressions for the characteristics simple enough so that boundaries are stable (Eq. A.5). During the second phase, which is dedicated to the study of the response of the wind to perturbations, we use full control of the incoming perturbations (Eq. A.7), and at the same time couple the magnetic potential ψ at the inner boundary with the potential ψ^0 obtained during the first phase (Eq. 7). Of course, we inject perturbations only after the system with the new method of control of boundary conditions (no incoming perturbations but full control and weak coupling with the potential) has relaxed.

2.4. Injecting Alfvén waves

Injecting perturbations via the characteristics method will inject fluctuations propagating at a speed which is locally the characteristic speed in the local plasma frame, namely, either the slow, fast, or Alfvén speed. We want here to inject Alfvén waves, this means that we will set $f_s^+(\theta,t) = f_f^+(\theta,t) = f_T^+(\theta,t) = 0$ in the rhs of Eq. (A.11,A.12,A.14), but $f_A^+(\theta,t) \neq 0$ in Eq. (A.13). Because the magnetic field is not normal to the boundary, the waves injected are not pure Alfvén waves neither in the linear sense (linear polarization) nor in the nonlinear sense (constant magnetic pressure). Nevertheless, we show now that the fluctuations injected via Alfvén characteristics are, at least in principle, close to arc-polarized Alfvén waves, i.e., to non-linear Alfvén waves, with a dominant linear (azimuthal) polarization.

To see it, we define the Elsaesser variables

$$z_\alpha^\pm = u_\alpha \mp sB_\alpha/\sqrt{\rho} \tag{8}$$

and also the formal time derivation operator:

$$\frac{\delta z_\alpha^\pm}{\delta t} = \frac{\partial u_\alpha}{\partial t} \mp \frac{s}{\sqrt{\rho}}\frac{\partial B_\alpha}{\partial t} \tag{9}$$

In the definition (8), the s factor is $s = sign(B_r)$; its presence ensures that, in the linear limit of radial propagation, z^+ denotes the amplitude of the upward propagating waves, and z^- that of the downward propagating waves. Note that $\delta z/\delta t$ is in general just an symbolic notation for the whole expression (9). It becomes equal to the derivative $\partial z/\partial t$ only in the linear limit, i.e. after replacing the density by its mean value in the expression for z. We also define for further use the normalized cross-helicity

$$\sigma_c = (z^{+2} - z^{-2})/(z^{+2} + z^{-2}) \tag{10}$$

Using the above notation, the equation at the inner boundary which describes the Alfvén wave injection reads (Eq. A1):

$$\beta_\phi \delta z_\theta^+/\delta t - \beta_\theta \delta z_\phi^+/\delta t = \epsilon A(\theta) C(t) \tag{11}$$

where ϵ is the perturbation amplitude, $\beta_\theta = B_\theta/B_\perp$ and $\beta_\phi = B_\phi/B_\perp$, where $B_\perp = (B_\theta^2 + B_\phi^2)^{1/2}$. A($\theta$) defines the variation of the injection with colatitude θ, and C(t) the time dependence. We choose $C(t)$ in order to obtain a monochromatic wave. More specifically, the factors $A(\theta)$ and $C(t)$ read in the case of runs A, C and E:

$$\begin{array}{l} C(t) = d/dt[f(t-t^0)sin(\omega(t-t^0))] \\ f(t) = 1 - exp(-(t/\tau)^4) \\ A(\theta) = sA^0(\theta)B/(\sqrt{\rho}\beta_\theta) \end{array} \tag{12}$$

The prefactor $f(t)$ is a ramp function which ensures that the average of the fluctuations is zero asymptotically. The associated transient lasts a time $\tau = \pi/(2\omega)$, i.e., a quarter of the period of the wave. This form is common to all runs. The function $A^0(\theta)$ is unity in the whole meridian (runs A and C), and zero at the poles, or unity in half a meridian (run E), and zero elsewhere (see Table 2). (Recall that the ϕ and θ components have to vanish at the poles, due to the axisymmetric condition). The factor $s = sign(B_r)$ leads to an abrupt change of sign at the equator, i.e., to a strong shear in the azimutal velocity field at the equator, but with a continuous B_ϕ. This choice is denoted by mode Su in Table 2. Mode Sb amounts to suppress the factor s in the definition of $A(\theta)$, in which case we have a shear of B_ϕ, instead of u_ϕ (run B in Table 2).

A last version of the injection mode has also been considered, in which the amplitude of u_ϕ is latitude-independent, with shear at the equator (instead of uniform B_ϕ/B (run D). This is mode Su', in Table 2).

Eq. (11) injects fluctuations with both the ϕ and θ polarizations, mixed in a complicated way. To obtain the relation between polarizations, we must consider the other boundary conditions. The other injection rates are zero. When the magnetic field is close to radial, one of the two magnetosonic characteristics equations (Eqs. A.11 or A.12, depending on sign of $v_a - c_s$), reduces to the following:

$$B_\theta \delta z_\theta^+/\delta t + B_\phi \delta z_\phi^+/\delta t = 0 \tag{13}$$

Now, if the reflected components z_α^- are negligible, we can replace in the last equation the z_α^+ terms by $-2B_\alpha$; then the equation reduces to a condition of constant modulus for the transverse field component

$$B_\theta^2 + B_\phi^2 = constant \tag{14}$$

or, equivalently (since in practice the radial component does not vary much), B^2 = constant. Hence, if no magnetosonic wave is injected, the Alfvén wave injection as defined in Eq. (11) corresponds approximately to a arc-polarized wave. If now the B_θ fluctuation is smaller than the mean component B_θ^0 (which in practice will be realized), we obtain

$$B_\theta^0 \delta B_\theta = -B_\phi^2/2 \tag{15}$$

which shows that the amplitude of B_θ is much smaller than that of the azimuthal component. Assuming a harmonic temporal variation, we deduce the relation between the standard deviations of B_ϕ and B_θ:

$$\sigma(B_\theta)/B_\theta^0 = 1/(2\sqrt{2})\sigma(B_\phi)/{B_\theta^0}^2 \tag{16}$$

Using $\beta_\theta \simeq 1$ and $\beta_\phi << 1$, which holds when the mean field is not too far from the radial direction, we derive from Eq. (11) that $\partial z_\phi^+/\partial t = 2\epsilon A^0(\theta)B/\sqrt{\rho}C(t)$. Hence, the standard deviation of the azimuthal component reads:

$$\sigma(z_\phi^+)/B = 2\epsilon/\sqrt{2}A^0(\theta) \quad (17)$$

(see below Fig. 8 a). Recall that $A(\theta)$ is unity in the emission region, and zero elsewhere. This gives us finally the approximate expression for the relative magnetic fluctuation: $\sigma(B_\phi)/B = \epsilon/\sqrt{2}A^0(\theta)$ valid when the mean field is not too far from radial and when downward propagating waves can be neglected.

Still considering the limit of quasi-radial field, the condition for no injection of slow or fast magnetosonic characteristics (again depending on the sign of $v_a - c_s$) degenerates to the plain downward propagating sound wave equation:

$$(1/\rho)\partial P/\partial t + c\partial u_r/\partial t = 0 \quad (18)$$

which, remembering that the flow is isothermal, c = constant, reduces to

$$\delta\rho/\rho = -\delta u_r/c \quad (19)$$

This characterizes a downward propagating acoustic mode. In practice, such waves could be generated because the injected Alfvén waves do not respect exactly the condition of constant pressure, and/or because pressure balance is destroyed as the wave propagates upward in the stratified atmosphere: the ϕ and θ polarizations should then evolve independently, and density fluctuations appear as one of the components of the linear magnetosonic eigenmodes.

The injected Alfvén wave has a wave period equal to 36 minutes. The relative amplitude of the Alfvén mode is $\epsilon = 0.14$ ("large amplitude") or 0.05 ("small amplitude"), see Eq. 17.

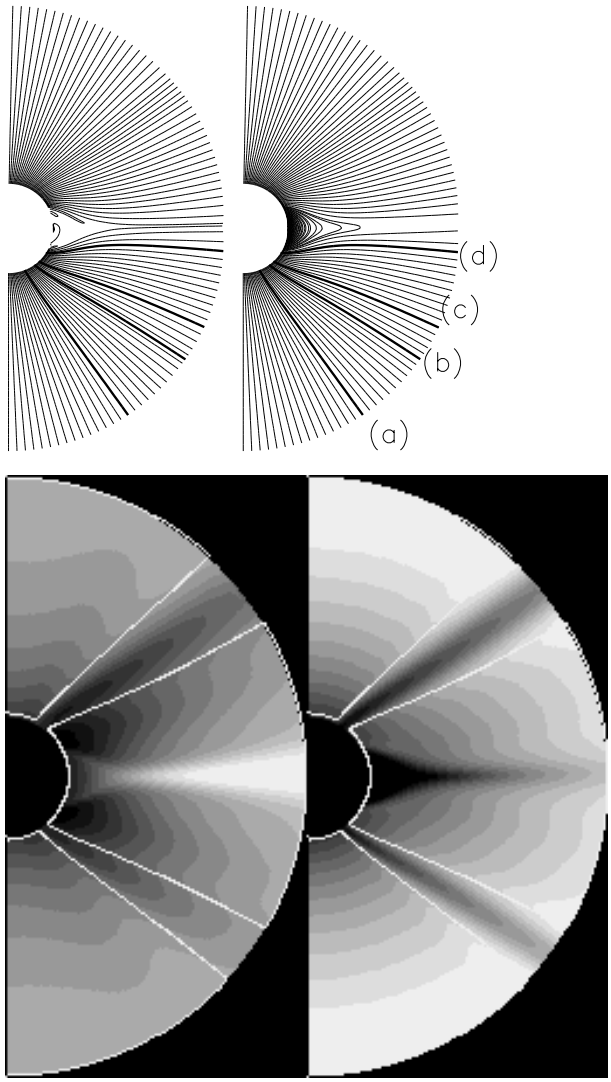

Fig. 1. Stationary wind with two cold streams (run C). Top: flow lines (left) and magnetic flow lines (right). Thick lines denote specific lines mentioned below in the rest of the paper by the labels (a), (b), (c), (d) (starting from the south). Bottom: density compensated for radial trend (left); radial velocity (right). Note that line (b) in the top figure is within the smallest cold stream shown in bottom figure. Temperature boundaries are materialized by white lines.

3. Results

The results are reported in the following order: first a global description is given, which allows a first comparison between the stationary and perturbed wind, then we consider more closely in turn the inner boundary, the closed loop region, and finally the open region.

3.1. The stationary wind versus fluctuating wind

Let us first describe the stationary wind with two cold coronal regions (run C, Fig. 1 and Fig. 2). The flow is characterized by a clear-cut partition of the domain between, on the one hand, the stagnant region and, on the other hand, the open flow region. The boundary between the two sub-domains takes the form of a so-called helmet streamer; it is characterized by large magnetic field gradients, i.e., large currents. Except along this boundary, (and even within the stagnant region where slow motions may exist) the flow lines are parallel to the magnetic field lines. Because magnetic and flow lines are not everywhere aligned, the pertinent definition of closed and open regions is not entirely clear. For instance, within the heliospheric current sheet where the stream lines are open, there are closed magnetic field lines advected by the flow, as shown in Fig. 1. To define closed lines, one might also rely on the Alfvén group velocity (sum of the Alfvén and bulk flow velocities): this would lead to defining the region where waves may propagate upward and return to the "ground". But we will see that waves actually return to the inner boundary again only in a very limited portion of this region. In the following, we will adopt as synonyms closed region and stagnant region.

The other structures with well-defined boundaries present in our study are the cold structures (runs C, D). The cold streams issued from the cold coronal regions are not conspicious when looking at the flowlines or magnetic field lines in Fig. 1; they

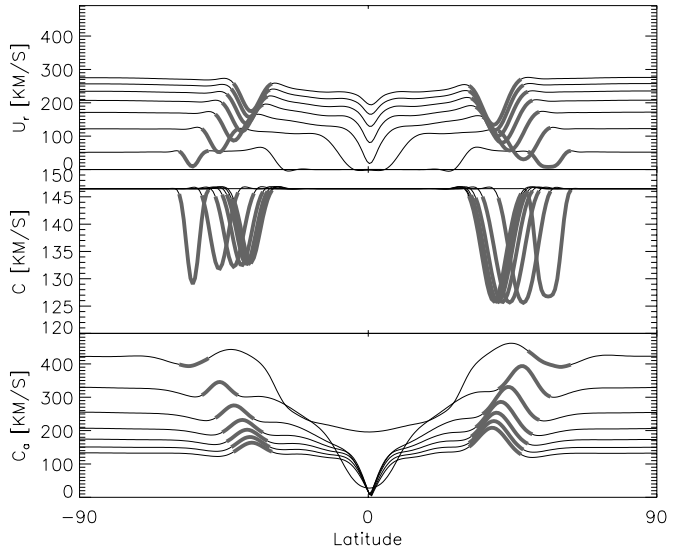

Fig. 2. Run C, unperturbed wind: profile of several quantities versus latitude at increasing distance from inner boundary, from 1.8 to 8.5 solar radii. Top: radial velocity; mid panel: sound speed; bottom panel: Alfvén speed (cold streams in grey). Note that u_r increases systematically with distance, while c_a decreases.

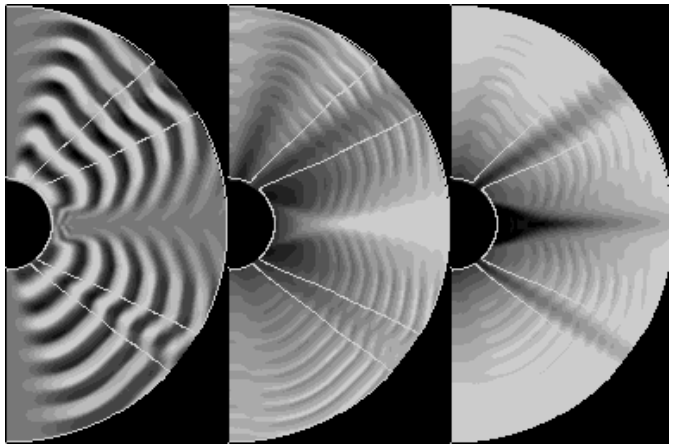

Fig. 3. Run C, wind perturbed by Alfvén waves. From left to right: main Alfvén wave (u_ϕ), density compensated for radial trend, radial velocity

only lead to a weak focusing of the lines, and also, indirectly, to a north-south asymmetry (because the south and north streams are of unequal sizes). The properties of the streams are apparent when looking at transverse profiles shown in Fig. 2. The streams are collimated toward the equator. Because the polytropic index is unity, the temperature is purely advected, which explains why the gap in temperature and sound speed (mid panel) within the streams remains constant with distance. The velocity gap of the streams (top panel) is on the contrary increasing with distance, and becomes rapidly larger than the bulk velocity gap in the current sheet: this is due to the sonic radius being larger than average within the streams.

The Alfvén speed (bottom panel) shows a peculiar behaviour when following a stream from the inner to the outer boundary. Close to the inner boundary, the Alfvén speed is smaller within the streams than average, and the density is larger. At a small height above the boundary, the magnetic field within the stream increases, which expells the matter, leading to an Alfvén speed excess, much larger within the largest of the two streams. Note that in this way the group velocity should not be very different within and outside the streams, which is confirmed by looking at the wave fronts of the perturbed wind (left panel in Fig. 3). The relative increase of the magnetic field within the cold streams, may be ascribed both to field stretching and to focusing of the streams; indeed, although the pressure at the inner boundary is the same ouside and inside the cold regions at the inner boundary, this pressure balance is destroyed as distance increases, see Grappin et al. 1997a).

Note that, although this cannot be guessed simply by looking at Fig. 1, cold streams modify the flow globally: a detailed comparison of runs A and C shows that the flow lines between a stream and the pole are (compared to the run A without streams) curved toward the stream, and, for the largest stream, the flow lines between the equator and a cold stream are also curved toward the stream.

Let us describe briefly the injection of Alfvén perturbations. Waves are injected during about 7 hours, i.e., about 13 wave periods. Snapshot pictures of u_ϕ, ρ (compensated for radial trend) and u_r after about 6 hours are shown in Fig. 3 in the case of run C. The figure may be compared with Fig. 1. The Alfvén perturbations are not injected at the poles, in order to respect the axisymmetry. Note that the wave front deviates in many places from radial symmetry, in particular in the vicinity of the ecliptic plane. Moreover, the waves are almost absent from a large region around the heliospheric current sheet (HCS).

The density and radial velocity also show fluctuations, with half the wavelength of the main wave. Note the emergence of a low-density structure between the largest cold stream and the pole: this new structure is generated by the interaction between the waves and the largest of the cold streams.

The global wave pattern is basically the same when the cold streams are suppressed. Only the wave front pattern is more regular, and the low-density structure is absent.

3.2. Inner boundary

We examine first the inner boundary because there we have an opportunity to test that the injected upward waves have the correct amplitude and properties. At the same time, we will be able to determine where there are reflected, downward propagating perturbations escaping the domain at the inner boundary.

Fig. 4 plots a snapshot of the u_ϕ and $B_\theta/\sqrt{(}\rho$ profiles for run A (no cold region) at a given time during the fourth Alfvén wave period. It shows that the two signals have the correct phase in the two hemispheres (the magnetic signal is even, the velocity is odd) and that the amplitudes of the velocity and magnetic field have the correct relation for an upward wave, for latitudes larger than 20^0. Closer to the equator, the superposition of upward and downward waves propagating along the closed loops naturally destroy these relations.

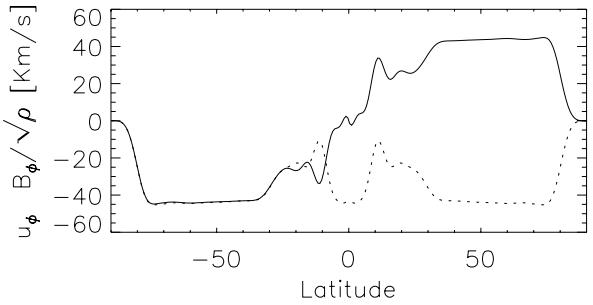

Fig. 4. Run A, Alfvén wave injection at inner boundary: snapshot profiles at $t = 101min$ of u_ϕ (continuous) and $B_\phi/\sqrt{\rho}$ (dotted)

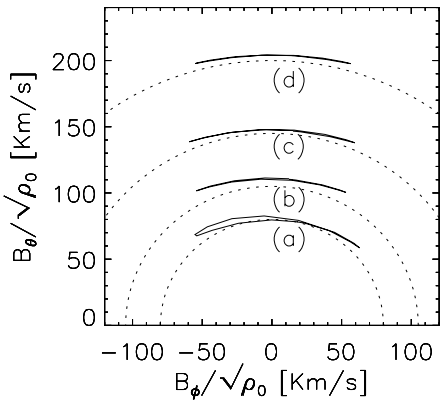

Fig. 5. Run C, hodographs of the magnetic field in the ϕ, θ plane, at the footpoints of the selected magnetic field lines (a) to (d) (see Fig. 1). Dotted points: circles for reference.

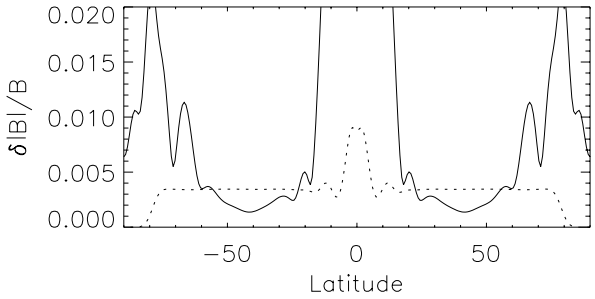

Fig. 6. Run A, relative rms variation of the magnetic field intensity $\delta|B|/B$. Note that the profile around the equator is meaningless, due to the long term oscillation of the B_θ component of the magnetic field in the closed loop region (see next figure). Dotted line: $1/(2\sqrt{2})/(\sigma(B_\phi)/B)^2$, which is the predicted amplitude for $\delta|B|/B$ for a purely linear (and harmonic) polarization.

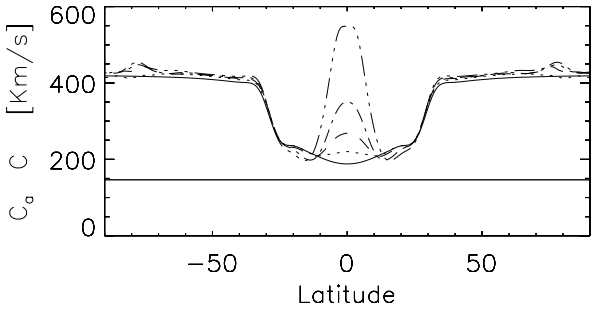

Fig. 7. Run A, long-term evolution of the inner boundary due to Alfvén waves gradients. Alfvén speed versus latitude at successive times, during 6.7 hours. Horizontal line: sound speed.

Hodographs of the magnetic field in the ϕ, θ plane are shown in Fig. 5 for run C at the footpoints of magnetic field lines (a) to (d) (see Fig. 1, namely at latitudes $69°, 55°, 48°$ and $34°$). It is seen that all hodographs trace portions of circle, corresponding well to relation 14. This ensures a almost constant magnetic field intensity in all places where the radial component of the magnetic field is constant. However, this is not the case everywhere, and in fact the standard deviation of the magnetic field intensity is lower than the one expected from the pure azimuthal (hence, linear) field variation only in the restricted latitudinal range 30 to $60°$, as shown in Fig. 6. The figure shows a huge peak within $\pm 20°$ of the equator. This peak in the magnetic intensity variation is to be interpreted with caution: it is not a measure of the short term oscillations of the field alone, as it also includes the contribution of a systematic drift of the poloidal (B_θ) field induced by the Alfvén wave injection.

This long-term drift is illustrated in Fig. 7. It corresponds actually to a long-period oscillation of the field, the period being about 10 Alfvén periods. The phenomenon is not generic, as it is the consequence of the particular choice of the latitudinal phase variation (shear of u_ϕ for run A). Indeed, the evolution does not occcur if the shear is suppressed or attenuated (as in run E, where a single hemisphere is perturbed, but the perturbation vanishing somewhat before the equator). Also, if the shear concerns B_ϕ instead of u_ϕ (run B), the evolution begins by a decrease of the B_θ component.

The relative amplitude (standard deviation) of the azimuthal magnetic field variation should be for run A about 0.1 from Eq. 17, since $\epsilon/\sqrt{2} \simeq 0.1$. All deviations from this should be interpreted as a signatude of downward propagating waves in the closed loops regions. Surprisingly enough, one sees in Fig. 8 (top, dotted curve) that the prescribed value, 0.1, holds everywhere but in a very small region of $\pm 10°$ around the equator. In contrast, the closed loop region itself is much larger, as shows the curve for the radial velocity (dashed curve) The same figure (top, continuous curve) also shows the upward propagating component, conveniently normalized: it corresponds to the correct value. The small dip at the equator is because the quasi-radial hypothesis used to derive relation (17) evidently breaks down here. The bottom panel of the figure shows the unnormalized upward and downward components, indicating that the downward component (dotted) is indeed restricted to the very center of the equatorial region.

The relative density fluctuations (not shown) is comparable or smaller than 2 per cent, depending on the latitudes. This is much larger than the magnetic field intensity fluctuation, which indicates that the perturbation is an acoustic wave propagating quasi-parallel to the mean field. It satisfies approximately relation (19), except within the center of the stagnation region. The source of these compressive downward propagating modes lies very close to the inner boundary, as the correlation between

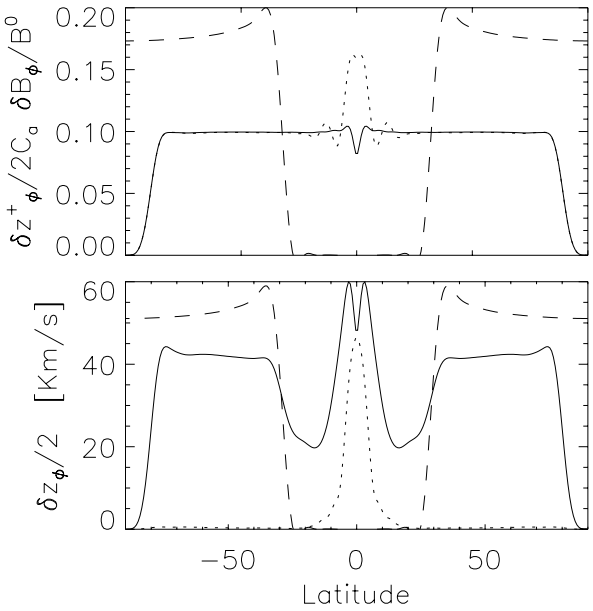

Fig. 8a and b. Run A, inner boundary: upward and downward wave amplitudes. **a** Normalized upward component and magnetic field amplitude: $(1/2)\sigma(z^+_\phi)$ (continuous) and $\sigma(B_\phi)$ (dotted), normalized respectively by the Alfvén speed and by the total magnetic field. **b** Upward and downward rms amplitudes: $(1/2)\sigma(z^+_\phi)$ (continuous) and $(1/2)\sigma(z^-_\phi)$ (dotted). The radial velocity field is superimposed (dashed) in arbitrary units on both panels, to mark the boundary of the stagnant region.

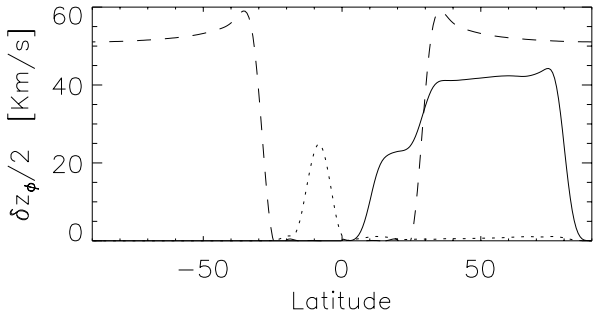

Fig. 9. Run E, inner boundary: transmission of Alfven waves from one hemisphere to the other. Rms amplitude of the upward $z^+_\phi/2$ (continuous) and downward component $z^-_\phi/2$ (dotted). Compare with Fig. 8, (bottom). Dashed line: radial velocity profile, showing the boundaries of the stagnant region

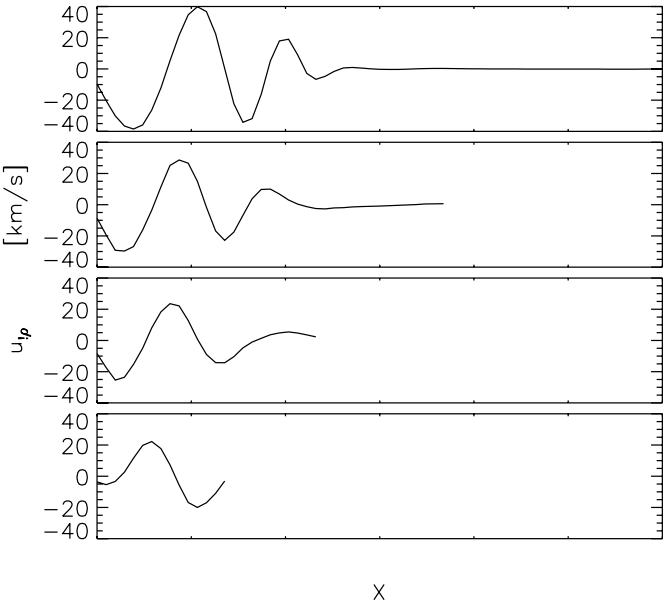

Fig. 10. Run E. Damping of Alfvén waves and reduction of wavelength along closed field lines. Snapshot profiles of u_ϕ versus coordinate X along field line (arbitrary unit). The loops are of decreasing length as their footpoints decrease in latitude from top to bottom: $\lambda = 26.5, 20.8, 15.2$ and $9.5°$.

radial velocity and density fluctuations changes sign after two or three mesh points. A reasonable source for these waves is the radial gradient of the magnetic field pressure associated with the upward propagating Alfvén waves.

3.3. The stagnant region

The long-term oscillation of the magnetic intensity observed at the boundary for the Alfvén waves with change of phase at the equator (condition Su) has a counterpart above in the closed loop region (not shown). A slow circulation develops, and the magnetic structure changes qualitatively, as it transforms, from an initially dipole-like structure, into an arch-structure with flux tubes with constant intensity along the tubes (and constant Alfvén speed). The cross-section of the flux tubes becomes constant. At the same time, a positive radial density gradient sets in, i.e., the magnetic arch structure supports a denser layer. This structure with very strong field intensity lasts for about ten Alfvén periods, as mentioned already in the last section.

Since this phenomenon is very dependent on the wave injection mode, we concentrate on a more generic problem, namely that of the wave transmission along the closed loops. We have seen that the downward propagating waves were not reaching the boundary, except very close to the equator, i.e., except when loops are very short.

To investigate what happens to the waves along a loop, we have considered waves emitted from one hemisphere alone (run E). We first plotted the z^+ and z^- standard deviations in Fig. 9; we see again that a small fraction of the wave reach the bottom boundary at the other hemisphere. To see in detail what happens to the wave along a given flux tube, we show in Fig. 10 snapshots of the wave profile along four loops of variable length regularly spaced from $9.5°$ up to $26.5°$. One sees that the wave is damped before returning to the ground, except for the shortest loop (bottom panel), and that for the loop close to the helmet streamer boundary (top panel), the wave damps before reaching the top of the loop. The damping goes along with a strong decrease in the parallel wavelength, due to a decrease in the Alfvén speed with heigth and with decreasing distance to the equator. Note that this is associated with a decrease of the perpendicular wavelength too, due to transverse gradients of the Alfvén speed.

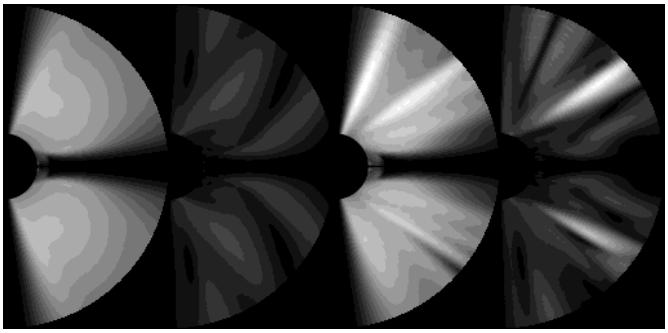

Fig. 11. Maps of rms wave amplitude. From left to right: run A (u_ϕ, u_θ); run C; (u_ϕ, u_θ). Intensity scaling is such that black corresponds to zero amplitude, and white corresponds respectively to 88 km s^{-1} for u_ϕ and to 43 km s^{-1} for u_θ. Note the large shadow cones around the equatorial current sheet.

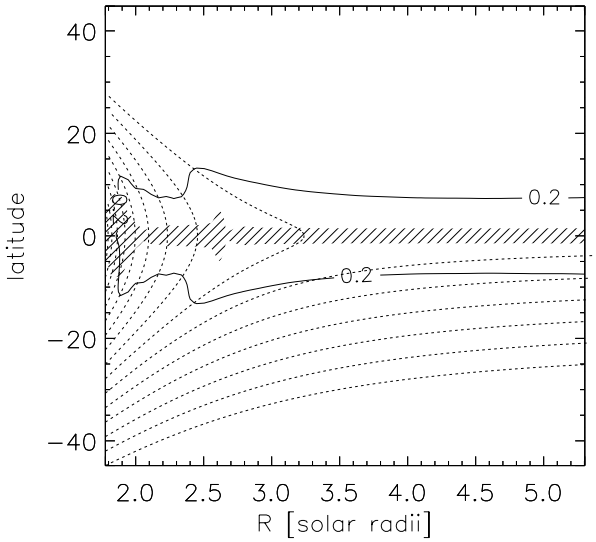

Fig. 12. Energy and cross-helicity σ_c in run A: close-up of the helmet streamer. Dotted lines: subset of the magnetic field lines before perturbation. Continuous contour: iso-amplitude of (z^+_ϕ) corresponding to the boundary of the shadow around the HCS, as seen in the previous figure. Dashed: region with cross-helicity lower than 80%.

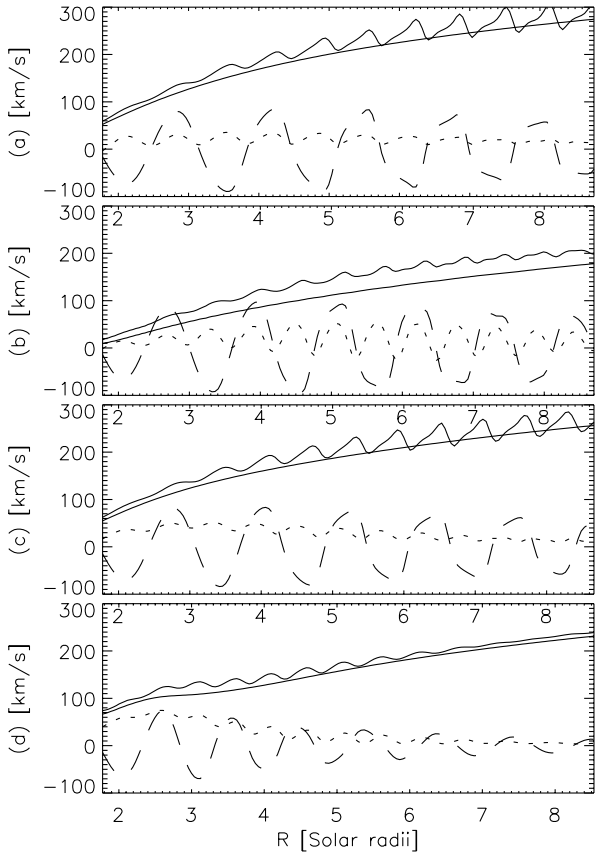

Fig. 13. Run C, snapshot profiles of the velocity components along the four selected open magnetic field lines, marked as thick lines in Fig. 1, top. The line (a) to (d) have decreasing latitudes ((a) is the closest to the south pole). Thick line: u_r just before wave injection. Other lines: snapshot profiles at 6.7 hours after beginning of wave injection; continuous: u_r; dotted: u_θ; dashed: u_ϕ.

3.4. Open field region

The open wind shows several distinct regions (see Fig. 1–3) which should affect in different ways the wave propagation and, in turn, their back-effect on the wind. Fig. 11 shows the contrasted views offered by the map of wave amplitude, separately the main (ϕ) and secondary (θ) components, with streams (two right figures) or not (two left figures). Brightness is proportional to the rms amplitude of the ϕ and θ velocity fluctuations.

Two features are apparent: the screening of a large region around the ecliptic for the main component, and the amplification of the secondary component within channels. Also, the main ϕ component is amplified within the new structure between the larger stream and the north pole.

A close-up of the helmet streamer is given in Fig. 12; a contour of the z^+ amplitude (in arbitrary units) is plotted, indicating the shadow cone where the wave amplitude is damped, with superposed magnetic field lines (dotted). The figure shows that the area where the signature of an upward propagating Alfvén wave is lost is very narrow, concentrated on the line where the magnetic field direction is undefined: the cross-helicity is smaller than 80% in the hatched region shown in the figure. In most of the domain, the cross-helicity is actually equal to about 1–10^{-3}. In contrast, the region around the heliospheric current sheet (HCS) where the wave amplitude is small is much larger: hence, the damping of the ϕ component is not associated with any wave reflection.

The forthcoming figures give radial and transverse profiles showing how the wave properties depend on distance and latitude. Fig. 13 shows snapshot profiles of the various velocity components (r, θ and ϕ) along the specific magnetic field lines (a), (b), (c) and (d) shown by thick lines in Fig. 1. From the south pole toward equator, the four field lines sample successively: (a) the region between south pole and the south cold stream, (b) the south stream, (c) the region between the stream and equator, and (d) a region in the vicinity of the heliospheric current sheet. Note that the field lines along which the sampling is made are defined

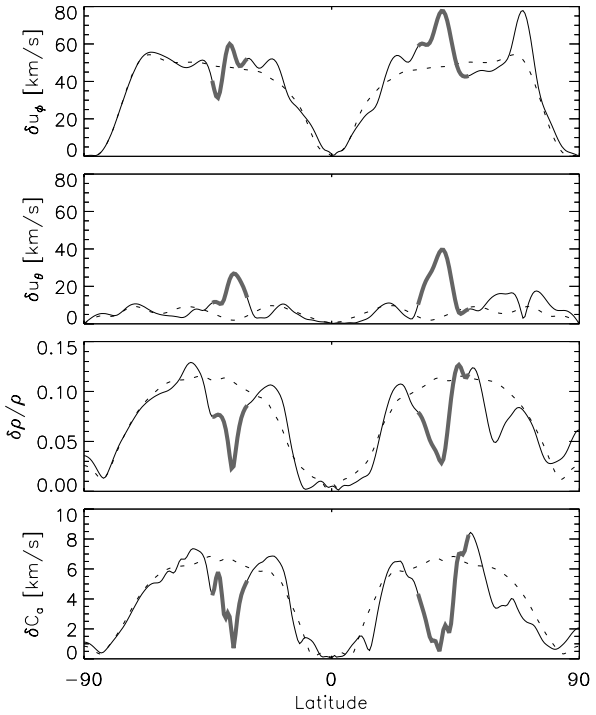

Fig. 14. Latitudinal profiles of standard deviations at $R = 7R_s$: comparison with and without streams. From top to bottom: u_ϕ, u_θ, relative density fluctuation, c_a (Alfvén speed). Dotted: no stream (run A); continuous: streams (run C), low temperature in grey.

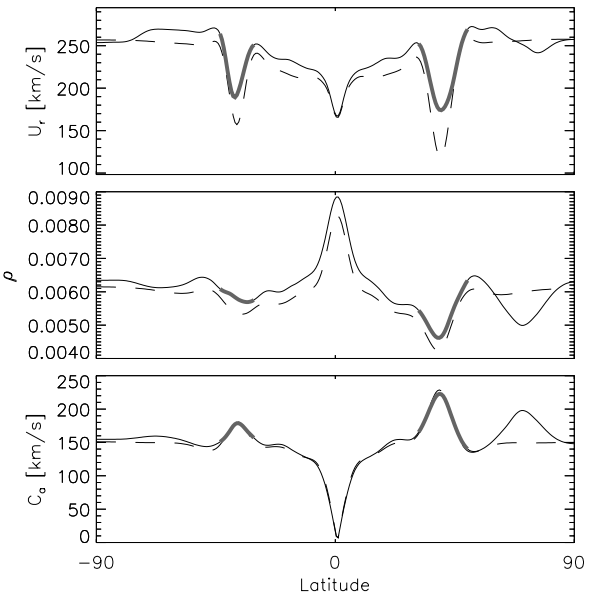

Fig. 15. Transverse cuts of mean plasma properties at $R = 7R_s$ (run C): Comparison with and without waves. Top: u_r; mid panel: density (arbitrary units); bottom panel: Alfven speed. Dashed line: profile before Alfvén wave; continuous (low temperature in grey): profile averaged during one wave period

using the group velocity, i.e. the flow velocity plus the Alfvén velocity, while the field lines shown in Fig. 1) are respectively the stream lines and the magnetic field lines.

The similarity between lines (a) and (c) indicates that, in the southern hemisphere at least, there are no more than three distinct regions: the homogeneous open wind, the streams, and the vicinity of the helmet streamer. The main features visible in Fig. 13 are: (i) inside the cold stream, the (compressible) wave associated with radial velocity fluctuations is much smaller than outside, the transverse wave amplitude (mostly the θ component) is larger, and the mean bulk velocity increase due to the wave is much larger than outside the stream; (ii) we see again that the main (ϕ) wave is strongly damped close to the helmet streamer.

The ecliptic region is not the only one with peculiar effects on wave propagation. Streams modify the distribution of the waves amplitude, both within and outside the streams, as seen in Figs. 11, the largest effect being observed in the vicinity of the large stream. This is shown more quantitatively in Fig. 14, in which rms quantities are plotted versus latitude in the developed wind, at about $R = 7$ solar radii. The figure shows that the θ component reaches within the large stream half the amplitude of the main (ϕ) component (see also Fig. 13). The ϕ component shows strong enhancements in the large stream, but strong variations above and below the standard level in the small stream. Note also the large enhancement close to the pole, within the secondary stream created by the interaction between the waves and the large stream. The same figure shows quantities related with the compressibility of the fluctuations. The rms amplitude of the density fluctuations is shown to decrease by a factor 10 in the center of the streams compared to the outside. The same is true for the fluctuations of the Alfvén speed, which is almost time-independent within the middle of the streams. Note that the magnetic field intensity also shows a minimum of its fluctuation level within the streams, but less pronounced than the Alfvén speed.

The modifications of the average wind properties induced by the waves are shown for the wind with streams in Fig. 15. There are two main effects: the modification of the average density profile associated with the new stream close to the pole, which is defined by a low density and a low magnetic field intensity (the Alfvén speed being unchanged), and the enhanced bulk speed increase shown within the streams. The latter reaches within the largest stream about 70 km s^{-1}, while outside it is not larger than 20 km s^{-1} (see also Fig. 10).

4. Discussion

In this section, we discuss in turn the acceleration due to the waves, the radial evolution of the wave amplitude, its polarization properties, and finally compare with solar wind properties.

4.1. Wind acceleration

We have seen (Fig. 15) that the radial momentum increase due to waves is larger within the streams than outside. To check whether this is a genuine effect due to the geometry of the stream or a simple consequence of the difference of the plasma parameters within the streams, we may compare the observed amplitude

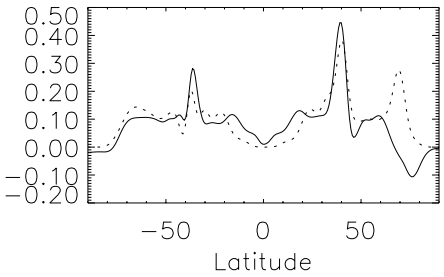

Fig. 16. Mean radial velocity increase due to Alfvén waves, at about 7 R_s, run C. Continuous: $(< u_r > -u_r^0)/c_s$, where u_r^0 is the radial velocity before wave injection. Dotted: $\sigma(u_\phi^2)/c_s^2$.

to the quasi- linear prediction. Quasi-linear analysis shows that the effect of the Alfvén waves on the mean wind speed, in the case of a radial mean magnetic field, appears as an additional pressure, whose magnitude is given by the magnetic energy contained in the fluctuations: δB_ϕ^2. A rough assessment of the quasi-linear prediction is thus provided by comparing the amplitude of the wind acceleration due to the wave $\Delta u =< u_r > -u_r^0$ to the square of the wave amplitude δu_ϕ^2, both normalized by the sound speed. (The brackets denote the velocity averaged over one wave period, and u_r^0 denotes the bulk velocity without waves). Fig. 16 shows a tranverse cut of both quantities at about $R = 7R_s$. There is a qualitative agreement between the two curves for most latitudes, and in particular within the streams. This indicates that the enhanced bulk speed within the streams is not due to a peculiar interaction due to the stream structure. There are however two regions where the two curves differ: the newly born channel, where the Alfvén wave energy has a strong peak, while the wind speed is in fact lower, and the heliopheric current sheet, where the momentum gain is positive while the wave amplitude is vanishing. In the former case, the explanation probably lies in the large deviation from radial expansion in the newly born channel which is strongly collimated. In the latter case, the transverse transport of radial momentum towards the ecliptic remains to be explained.

4.2. Wave amplitude and cross-helicity

The WKB prediction for the wave amplitude holds when two conditions are satisfied: dissipation should be small, and the frequency should be higher than the frequencies associated with the large scale gradients. We consider in turn the two conditions. The first condition, small dissipation, holds holds when the wave number is significantly larger than the dissipation scale, here the mesh size. The second condition requires in particular that the Alfvén frequency $\omega_A = kv_a$ (measured in the plasma frame) be higher than the expansion rate, the ratio being measured by the small parameter:

$$\eta = (\partial V_a/\partial r/2 + divU^0/4)/\omega_A \tag{20}$$

(Velli et al., 1989). In that limit, the wave rms amplitude should follow the WKB prediction:

$$\delta u_\phi \simeq \delta B_\phi/\sqrt{(}\rho) \simeq \sqrt{u_r v_a}/(u_r + v_a) \tag{21}$$

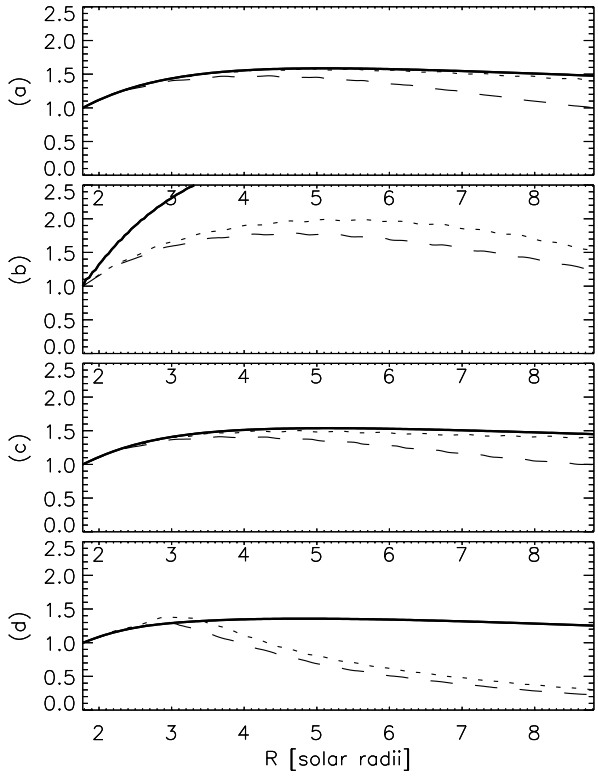

Fig. 17a–d. Large and small amplitude Alfvén wave evolution compared to WKB prediction, rms u_ϕ profile along the four selected field lines **a**, **b**, **c** and **d** (see Fig. 1). Continous: WKB prediction; dotted: small amplitude (run D); dashed: large amplitude (run C). All amplitudes are normalized to unity at the basis of the magnetic field line.

and, also, the deviation from maximal cross-helicity remains small, since

$$z^-/z^+ \simeq \eta \tag{22}$$

With the frequency considered here, we have in most of the domain $\eta \simeq 0.02$, which leads to $\sigma_c \simeq 1$–10^{-3}, corresponding well to the measured value outside the HCS.

The dissipation should initially be negligible, as the wavelength is initially about 20 mesh sizes. Hence one should observe the WKB prediction for amplitude evolution, at least close to the inner boundary. However, it is clear from Fig. 13 that u_ϕ shows significant steepening along flux tubes (a) to (c): a substantial part of the wave energy goes into scales close to the mesh size, hence should be dissipated by the numerical filtering. In contrast, in flux tube (d), closest to the current sheet, the wave shows no steepening but a much more rapid decay.

In order to be able to discriminate between the causes of eventual departures from the WKB evolution, we have compared the WKB prediction (Eq. 21) with the rms amplitude of the main (u_ϕ) component both for run C, and the low amplitude case (run D) for which no steepening is expected during an advection time (Fig. 17). The profiles are shown again along the four lines (a) to (d), and are normalized to unity at the footpoint of each line. One observes that:

1. Along lines (a) and (c), the small-amplitude wave follows about exactly the WKB prediction, while the large- amplitude wave shows substantial damping.

2. Along line (b), the wave profile is comparable to that along (a) and (c); but much lower than the WKB expression, which is here much higher than along (a) and (c), due to the much smaller value of the ratio u_r/v_a within the stream. Note that the disagreement is not unexpected, since the WKB approximation looses meaning within the streams, as the wavelength is there comparable to the stream size (see Fig. 3.

3. Along line (d), the large and small-amplitude profiles are comparable; they both first follow the WKB profile, then suddenly deviate strongly from the WKB profile, after about 3 solar radii.

A plausible interpretation is as follows: along lines (a) to (c), the damping is due to nonlinear steepening, while along (d), the damping is due to a linear effect, as it does not depend on wave amplitude. This effect is the phase mixing, i.e., the shear of the wavefronts due to the transverse gradients of the phase velocity, which is the sum of the Alfvén speed and wind bulk speed. If one examines, along line (d), the transverse gradient of the phase velocity $u_r + v_a$, one sees that it has indeed a strong maximum around 3 solar radii, precisely the distance where the wave amplitude abruptly starts to dissipate (Fig. 17). Along the lines (a) to (c), the transverse gradients are everywhere an order of magnitude smaller.

The Alfvén speed gradient is also responsible of the damping in the stagnant region (cf. Fig. 13, 17). The shear of the wave fronts lead to damping because, by tilting the wavefront, it decreases the wavelength.

While in a plane parallel shear flow, there is no limit to the decrease of the wavelength due to the shear of the wave front, in an expanding wind, there is a minimum wavelength $\lambda_\perp$, which in a spherically expanding wind is given by:

$$\lambda_\perp/\lambda \simeq V/(\partial V/\partial\theta) \qquad (23)$$

λ being the initial radial wavelength, and V the phase velocity, here $u_r + v_a$ (Grappin & Velli, 1996). When taking into account the steep transverse gradients close to the boundary between the stagnant and the open flow region, one finds that this leads to $\lambda_\perp/\lambda \simeq 0.2$, which is compatible with a visible inspection of Fig. 3. This is about four radial mesh points for $\lambda_\perp$, or about the same number of transverse mesh points (note that initially the transverse mesh size is smaller than the radial size, but this changes around 3 solar radii).

4.3. Oblique or parallel wave? Linear or arc polarization?

Apart from the amplitude decrease of the main wave, there are two more properties of the wave which we would like to investigate here, namely the variation of the modulus (is the Alfvén wave an arc-wave?) and the direction of minimum variance: is the minimum variance aligned with the mean field?

If we simplify and consider purely monochromatic waves, the first property is a property of oblique waves, while the second characterizes parallel waves. Indeed, parallel waves, i.e., waves with their wavevector aligned with mean field, have by definition (since div$B = 0$) their minimum variance direction aligned with the mean field, while oblique waves, i.e., waves with an angle $\theta(k, B^0)$ large enough, leads to a secondary component in the plane (k, B^0) which compensates to second order the variation of the modulus of the magnetic field (Fig. 18), as first shown by Barnes & Hollweg (1974). Note that B^0 denotes

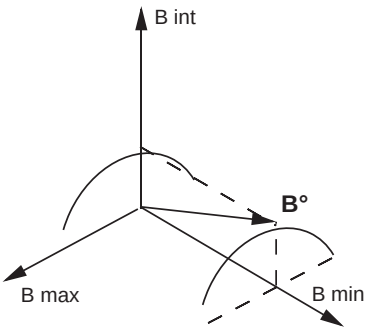

Fig. 18. Arc-polarized wave conserving the magnetic intensity. B^0 is the unperturbed magnetic field. The coordinates (Bmin, Bint, Bmax) are respectively the directions of minimum, intermediate and maximum variance of the matrix $< \delta B_i \delta B_j >$. Here Bmax is the azimuthal magnetic field component, and the plane plane (Bmin,Bint) coincides with the (B_r, B_θ plane: in principle, at the inner boundary Bmin is B_r, and Bint the B_θ. However, even at the boundary, there are fluctuations of B_r, hence the minimum variance direction deviates from the radial (see text).

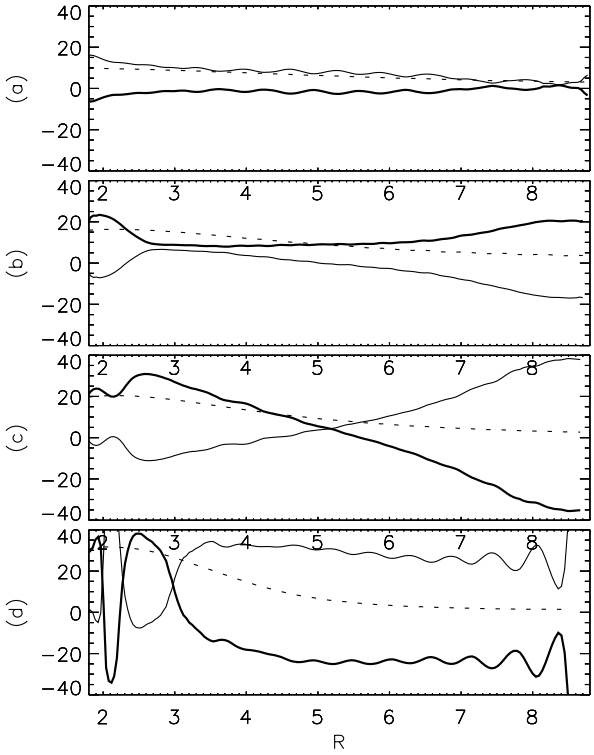

Fig. 19a–d. Run C, characteristic angles along the four characteristic lines **a**, **b**, **c** and **d** (see Fig. 1). Continuous: α; dotted: δ; thick: $\theta(B^0, \kappa)$ (see Eq. 24).

here, at variance with the notation used in Sect. 2, the total unperturbed field. In the following, B^0 will denote the time-averaged magnetic field, which in principle is the same, to first order in the perturbation (see Fig. 18).

In the solar wind, the spectrum is rich, i.e., waves are not monochromatic plane waves, and this is why one can observe at the same time properties which would seem to be contradictory, characterizing either parallel, or oblique waves.

Here, the situation is intermediary: the main Alfvén wave is initially monochromatic, but does not completely remain so, because of the large-scale gradients and nonlinear coupling. Hence it is interesting to ask what properties characterize the simulated waves. and in particular whether, if the conditions are met to obtain an oblique wave, one finds a constant modulus Alfvén wave, even though the medium is inhomogeneous and stratified.

Note that the initial (boundary) configuration of the wave is, in principle, close to the constant modulus (oblique) wave, see Eq. (15). However, in practice, we have seen that, due to the transverse modulation of the amplitude, a radial component also exists which breaks the conservation of the modulus in a large latitude interval. Hence the boundary condition is not uniform, and one may ask two questions: a) when the boundary condition is of constant modulus, does it remain so at larger distances, b) when not, does it relax to such an arc-Alfvén wave?

Let us first answer a simpler question: is the wave oblique or parallel? Fig. 19 shows the three basic angles in the meridional plane which allow to answer the question:

$$\alpha = (\kappa, \hat{e}_r), \qquad \delta = (B^0, \hat{e}_r), \qquad \theta(B^0, \kappa) = \delta - \alpha \qquad (24)$$

One sees that the answer depends strongly on the starting latitude of the field line. Along line (a), the direction of minimum variance and the mean field direction both vary together, so that the wave is rather close to being parallel. At the same time, the secondary component, namely δB_θ, decreases as the main component, i.e. following approximately the WKB prediction, apart for some dissipation. It happens that this field line is (by coincidence) about the only one for which this is the case: as a rule, the angle $\theta(\kappa, B^0)$ is significantly different from zero, and the amplitude of the secondary component deviates strongly (generally by an order of magnitude) from the WKB prediction.

In fact, the most common behaviour is that of line (c), for which the angle varies strongly within the domain. As a consequence, no relaxation is possible, so that neither the parallel behaviour (with WKB decrease for the secondary component) nor the oblique behaviour (with constant modulus) is possible.

In contrast, the behaviour along lines (b) and close to the current sheet (d) is exceptional: there the wave is constantly oblique. However, in the case of line (d), the damping is very strong, so that it is difficult to expect the relaxation towards the constant modulus state predicted by Barnes & Hollweg (1974).

Fig. 20 shows the hodograms of the magnetic field during one wave period, at about 7 solar radii, on lines (a) to (d). One sees that the only line where the secondary component is able to compensate well for the variation of the magnetic field modulus due to the main (ϕ) polarization is line (b).

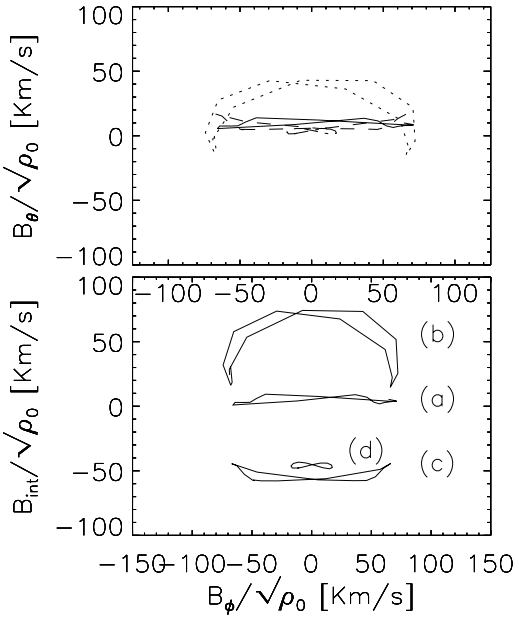

Fig. 20. Run C, hodographs of the magnetic field at about 7 solar radii, on lines (a) to (d). Top: $B_\phi/\sqrt{\rho^0}$ versus $B_\theta/\sqrt{\rho^0}$; continuous: (a); dotted: (b); dashed: (c); dotted dashed: (d); Bottom: $B_\phi/\sqrt{\rho^0}$ versus $B_{int}/\sqrt{\rho^0}$

This does not mean that the coupling between the main polarization (ϕ) and the others, as found by Barnes & Hollweg (1974) is absent in general. As is shown in Fig. 20 (c), when the wave is oblique but when the angle is changing too fast, the secondary component (δB_θ) indeed compensates somewhat for the modulus variation, but typically not enough, so that the modulus fluctuation remains comparable to the level expected for a purely linear polarization. Note that, because the wave steepens with distance, the variation both of the secondary component and of the modulus become concentrated during a shorter time interval, so that the rms variation of the modulus decreases somewhat with distance, compared to that expected for a sinusoidal wave with linear polarization.

4.4. Solar wind versus simulations

In the wind, the level of the normalized cross-helicity σ_c, which is the signature of purely upward propagating Alfvén waves, is decreasing when one approaches the heliospheric current sheet (HCS). But the interpretation of this sole observation is not evident: one may have either generation of magnetosonic waves, or generation of downward propagating waves. In fact, one also observe at the same time a larger relative density fluctuation, which is in favour of the former hypothesis. This transformation of Alfvén waves into magnetosonic waves is nicely described by Malara's scenario (Malara et al., 1996). In this scenario, the waves are initially already present in the HCS. In reality, they come from the sun, and have to first propagate through the corona to arrive there. This is what happens in the present work, and in that case we have seen that the wave energy is dissipated during the propagation, well before reaching the HCS, This is

done without any substantial decrease of the normalized cross-helicity, nor any increase of the relative density fluctuation. In fact, Fig. 14 shows that fluctuations vanish for all degrees of freedom in a large region around the HCS.

One could think, of course, that the damping by phase mixing is largely exaggerated in the simulation, compared to the real solar wind, in view of the large factor (an order of magnitude) between the mesh size and the proton gyration radius (which are indications of the ratio of the dissipative scales, respectively in the simulation and in the real wind). However, the real problem (both in comparison of the real wind and in comparison of Malara et al.'s simulations) is the absence, in our simulations, of decrease of σ_c, and the absence of increase of $\delta\rho/\rho$.

Why is it so? A first point is that in the present simulations, the Alfvén waves are purely (or mainly) (oblique) Alfvén waves in the true linear sense, while in Malara et al.'s simulations they are initially parallel waves which are in fact fast magnetosonic waves as soon as the propagation ceases to be parallel (Malara, personal communication). The latter situation could be more representative of the real wind. A second possibility is that the HCS might be turbulent, which would provide for a direct source of non-Alfvénic waves. Although this is an attractive hypothesis (see Grappin & Léorat 1998, and Einaudi et al. 1999 for a complete study of the homogeneous case), the first hypothesis is more tempting, again because Malara's scenario meets the observations with some success.

Let us turn to the high latitude regions far from the HCS. Another main point of this work is that, in such regions, the waves are arc-shaped, (i.e., nonlinear Alfvén waves with quasi-constant pressure) only within peculiar structures, the streams generated by cold coronal regions. In these regions however, the WKB prediction is completely false, due to the small size of the structure. One could be tempted to enlarge the size of the structure in order to recover the WKB decay, but it is plausible that by doing so we would lose the wave-guide property which maintains a constant oblique angle and is at the origin of the arc-shape property.

Hence, far from the HCS, we have either a reasonably WKB-like behaviour (apart from dissipative damping due to nonlinear steepening), or arc-shaped waves, but not both properties at the same time. This is at variance with the real wind, where both properties hold. Two hypothesis are possible. First, this regime may be transient, i.e., the situation may relax at larger distances, be only because the spiral forms, which should imply that the propagation becomes generally oblique (not only within structures). But nonlinear coupling seems to lead to the minimum variance direction being parallel to the mean field in the wind, so that the propagation is in average at least parallel, not oblique... A second (in fact complementary) hypothesis is that the situation be complex: the spectrum is a continuous distribution of directions of wavevectors, so that the average wavevector direction is parallel to the mean field, but the oblique wavevectors have enough weight for the oblique regime of Barnes & Hollweg (1974) to hold. Also, note that the fact that the wave amplitude does not follow the WKB radial profile within the stream (while solar wind waves do) does not prove that such streams do not exist; in fact, possible peculiar wave profiles within streams may not appear in the statistical averages made in the wind, due both to the method of sampling and to the relative weight of the streams in the global wind.

A last point is how fluctuations affect the mean plasma state. The birth of an additional stream structure close to the largest stream, and also the long-term oscillations and strong field build-up observed around the equator in the closed loop region show that, even when the wave flux is small, the coupling between polarizations can take unexpected forms, which deserve to be studied independently. In open field regions, the classical quasi-linear effect of the wave pressure is seen to work correctly in the present simulations. To be in a position to study more pronounced effects, leading to fast winds, one should consider extending the numerical domain to smaller radial distances, to include the stratified region, to allow for large increase of the wave amplitude; second, one should consider richer spectra both in direction (wave vectors) and frequencies, including in particular the lower frequencies which seem to be a particularly efficient way to transfer momentum to the wind (Lau & Siregar, 1996; Ofman & Davila, 1998).

5. Conclusion

We considered the problem of the propagation of Alfvén waves in an axisymmetric wind, in the accelerating region. The heating problem is not considered, but the exchange of momentum is fully taken into account, both in the open flow and the closed loop regions. In this work, only monochromatic waves are considered. The rotation of the sun is not taken into account, so that the average azimuthal magnetic field is zero.

Two main results emerge. First, the waves remain remarquably purely Alfvén waves, as far as the signature of the cross-helicity is concerned. This remains true even very close to the heliospheric current sheet. The Alfvén wave flux is very low in a large region around the current sheet, not because the waves have decayed into other wave modes or polarizations, but because of the damping to the shear of the wave front due to transverse gradients in the plasma bulk properties (bulk speed and Alfvén speed).

Second, the two main properties characterizing Alfvén waves far from the HCS, namely a) the small fluctuation level of magnetic field intensity b) the approximate WKB amplitude decrease, do not hold both in a given region of the simulated wind. In the wind with no additional structure (i.e., no cold stream), the wave decrease is approximately WKB (apart from some additional decay due to nonlinear wave steepening), but the modulus of the magnetic field is approximately that expected from a linear polarized waves, because the magnetosonic polarization is not large enough. Only within the cold streams does the wave become a constant modulus arc-wave in the sense of Barnes & Hollweg (1974). But in this case, the wave radial profile is drastically deviating from the WKB prediction, at variance with the average behaviour observed in situ.

The fact that the arc-wave property is not easily recovered in the simulated wind, while it is easily obtained for oblique waves

propagating in a homogeneous medium, could come from the fact that the angle between the mean field and the minimum variance direction (the local wave vector) is varying with distance. The angle remains reasonably constant (and oblique) only within the structured (cold) streams, which act as wave guides.

It is tempting to imagine that the wind is filled with such structured streams, akin or not to the ones considered here, but there remains the problem of how to recover the average WKB behaviour of the waves observed in situ.

The solution might be of course that the present results are here specific of the distance range considered, i.e., that everything changes at larger distances. For instance, the WKB radial profiles might be recovered within streams at larger distances, since the difference in Alfvén Mach number between the stream and the ordinary plasma should decrease. But the question then is whether the streams still act as wave guides, i.e., whether the waves remain oblique enough to have a vanishing level of magnetic intensity fluctuations.

On the other hand, it is tempting to insist in working within the accelerating region because, again, the constraints imposed by the sonic surface prevents one from playing too freely with the plasma parameters. In that line, it is urgent to look for less deterministic situations with a distribution of wave vectors, and to investigate in a general way the mechanism which lead to a dominance of oblique waves in the wind.

Acknowledgements. We thank F. Malara and M. Velli for fruitful discussions, and IDRIS for providing numerical facilities (project 990219).

Appendix A: boundary conditions

To specify the boundary conditions, we have to recast the equations in a form (called the characteristic form) which shows which information goes into the domain and which information goes out of the domain. The former has to be specified, the latter must be computed in the same way as inside the numerical domain. The method is recalled briefly here, since there are some points which are not fully documented in the litterature. To begin with, we write formally the MHD equations for all terms except B_r as:

$$\frac{\partial X}{\partial t} + A\frac{\partial X}{\partial r} = C\frac{\partial X}{\partial \theta} + D \tag{A.1}$$

where X is a vector with 7 components: $(\rho, T, u_r, u_\theta, u_\phi, B_\theta, B_\phi)$ and D is a matrix representing terms which contain no derivatives, i.e., curvature terms, gravitation, and dissipative terms. We do not include the equation for B_r as the equation for B_r does not show any derivative with respect to r. Hence it does not correspond to information propagating through the boundary: nothing concerning B_r has to be specified there.

The matrix A has 7 eigenvalues λ_i, which are:

$$\lambda_1 = u_r$$
$$\lambda_2 = u_r + v_a \quad \lambda_3 = u_r - v_a$$
$$\lambda_4 = u_r + v_s \quad \lambda_5 = u_r - v_s$$
$$\lambda_6 = u_r + v_f \quad \lambda_7 = u_r - v_f$$

where v_a, v_s, v_f are the Alfvén, slow and fast speeds. The first eigenvalue corresponds to the entropy mode (pressure-balanced), which is just advected. We now define the left eigenvector Y_i:

$$Y_i A = \lambda_i Y_i \tag{A.2}$$

where the normalization of the Y_i is conveniently chosen so as to prevent as much as possible the occurence of singularities in the final equations ((Hu & Wu 1984, Brio & Wu 1988, Vanajakshi et al. 1989).

Now, Eq. (A.1) may be projected in turn on each eigenvector Y_i, which leads to the following system (i=1...7):

$$Y_i \partial X/\partial t + L_i = Y_i C \partial X/\partial \theta + Y_i D \tag{A.3}$$

Replacing L_i by the expression

$$L_i = \lambda_i Y_i \partial X/\partial r \tag{A.4}$$

in Eq. (A.3) leads to a set of equations exactly equivalent to the original equations A.1, if we add the conditions of zero divergence to specify B_r. Now, we use Eq. (A.4) at boundary points where the eigenvalue λ_i is negative (let us be specific and consider only the inner boundary), i.e., where the information is coming out of the medium, in which case we consider that no extra-information is necessary. At the other points, i.e., where the eigenvalue λ_i is positive, we specify the incoming information by specifying the value of the characteristic term L_i. Once this is done, all fields depend in general on this choice, as the evolution equations of the fields X depend on complex combinations of the characteristic terms L_i, obtained by unprojecting Eq. (A.3). Note that the unprojected equations are not written for conciseness.

We have several possible choices for the control of the incoming information. A first (wrong) choice would be to replace the incoming L_i as well (hence whatever the sign of the eigenvalues) by the expression A.4; this would bring no information from the external medium, leaving the boundary with no constraint, entirely dependent on the interior; it is insufficient to obtain numerical stability. At least some information must be specified at each boundary point, in fact as much as the number of positive eigenvalues λ_i.

A better choice is to replace each incoming L_i by a specific function:

$$L_i = -f_i(\theta, t) \tag{A.5}$$

This leads to the projected equation:

$$Y_i \partial X/\partial t = f_i(\theta, t) + Y_i C \partial X/\partial \theta + Y_i D \tag{A.6}$$

This choice does clearly not lead to the total control of the incoming perturbations. In practice, such conditions are useful, because they are very stable, in the phase of wind building, i.e., to obtain a stationary wind, using a time-independent f_i. However, this is not a good choice for the further investigation of the response of the wind to time-dependent perturbations, as the perturbation triggered by the function f_i propagates along

the boundary, due to the derivatives with respect to θ remaining in the rhs, without their radial derivatives counterparts. This propagation is not physical, i.e., it is entirely a product of the boundary condition. Intermediate conditions (i.e., absorbing the transverse derivatives in the characteristics, but not the curvature terms D) have been considered (Grappin & Léorat, 1998), but the total control of incoming perturbations is certainly preferable. Its drawback is that it is a source of instability. This instability has been cured here by careful adjustment of the numerical scheme, to be described elsewhere.

The total control of the incoming perturbation amounts to choose for the L_i:

$$L_i = -f_i(\theta,t) + Y_i C \partial X/\partial\theta + Y_i D \tag{A.7}$$

As a result, the final projected equations become:

$$Y_i \partial X/\partial t = f_i(\theta,t) \tag{A.8}$$

Eq. (A.8) holds at all points of the boundary where λ_i is positive. Elsewhere, we use as already said the natural (interior) expression (A.4) for the characteristic terms L_i instead of Eq. (A.7).

In practice, the characteristic equations are not integrated directly; instead, the equations for the fields $\rho, T, u_r, u_\theta, u_\phi, B_\theta, B_\phi$ are integrated, but modified by first incorporating the boundary conditions in the rhs of the field equations. This is done by expressing the field equations in terms of the characteristics L_i (i.e., unprojecting equations (A.3)), after replacing the characteristics L_i either by the natural expressions (A.4) or by the specific expressions (A.7), depending on the sign of each eigenvalue. Formally, this may be written:

$$\partial X/\partial t + \Sigma Z_i L_i = C\partial X/\partial\theta + D \tag{A.9}$$

where the Z_i are the right eigenvectors of the matrix A.

Let us be now specific, and consider the case of the response to incoming perturbations of a stationary wind with subsonic regime at the inner boundary, and supersonic regime at the outer boundary. More precisely, assume that the bulk speed is nowhere negative and is everwhere smaller than the slow speed everywhere at the inner boundary. Then there are at all points of the inner boundary four positive eigenvalues, i.e., four incoming characteristics: slow, fast, Alfvén and entropy. To write the explicit boundary conditions, we need to define the following notations:

$$\begin{aligned}
&V_a = abs(B_r)/\sqrt{\rho}\\
&s = sign(B_r)\\
&\beta_\theta = B_\theta/(B_\theta^2+B_\phi^2)^{1/2}\\
&\beta_\phi = B_\phi/(B_\theta^2+B_\phi^2)^{1/2}\\
&\alpha_1 = [(v_f^2-v_a^2)/(v_f^2-v_s^2)]^{1/2}\\
&\alpha_2 = [(v_f^2-c^2)/(v_f^2-v_s^2)]^{1/2}\\
&\delta x_i^+/\delta t = \partial u_i/\partial t - (s/\sqrt{\rho})(c/v_f)\partial B_i/\partial t\\
&\delta y_i^+/\delta t = (v_a/v_f)\partial u_i/\partial t - (s/\sqrt{\rho})\partial B_i/\partial t\\
&\delta z_i^+/\delta t = \partial u_i/\partial t - (s/\sqrt{\rho})\partial B_i/\partial t\\
&\delta u^+/\delta t = (1/\rho c)\partial P/\partial t + (v_s/c)\partial u_r/\partial t\\
&\delta v^+/\delta t = (1/\rho v_f)\partial P/\partial t + \partial u_r/\partial t
\end{aligned} \tag{A.10}$$

The explicit equations describing the incoming perturbations at the inner boundary are then for the slow, fast, Alfvén and temperature perturbations (resp. for L_4, L_6, L_2 and L_1):

$$\alpha_2\delta u^+/\delta t + \alpha_1 s(\beta_\theta \delta x_\theta^+/\delta t + \beta_\phi \delta x_\phi^+/\delta t) = f_s^+(\theta,t) \tag{A.11}$$

$$\alpha_1\delta v^+/\delta t - \alpha_2 s(\beta_\theta \delta y_\theta^+/\delta t + \beta_\phi \delta y_\phi^+/\delta t) = f_f^+(\theta,t) \tag{A.12}$$

$$\beta_\phi \delta z_\theta^+/\delta t - \beta_\theta \delta z_\phi^+/\delta t = f_A^+(\theta,t) \tag{A.13}$$

$$\partial T/\partial t - (\gamma-1)T/\rho\partial\rho/\partial t = f_T(\theta,t) \tag{A.14}$$

References

Alazraki G., Couturier P., 1971, A&A 13, 380,

Barnes A., 1966, Phys. Fluids 9, 1483

Barnes A., J.V. Hollweg, 1974, J. Geophys. Res. 79, 2302

Buttighoffer A., Lanzerotti L.J., Thomson D.J., Maclennan C.G., Forsyth R.J., 1999, A&A 351, 385

Buttighoffer A., Pick M., Roelof E.C., et al., 1995, J. Geophys. Res. 100, 3369

Brio M., Wu C.C., 1988, J. Comput. Phys. 75, 400

Einaudi J.G., Boncinelli J.P., Dahlburg J.B., Karpen J.J., 1999, J. Geoph. Res. 104, 521

Grappin R., Mangeney A., 1996, Solar Wind 8, AIP Conf. Proc. 382, p. 250

Grappin R., Léorat J., Cavillier E., Prigent G., 1997a, A&A 317

Grappin R., Cavillier E., Velli M., 1997b, A&A 322, 659

Grappin R., Léorat J., 1999, In: Habbal S.R., Esser R., Hollweg J.V., Isenberg P.A. (eds.) Solar Wind Nine. AIP Press, Woodbury, N.Y., p. 333

Grappin R., Velli M., 1996, J. Geophys. Res. 101, 425

Grappin R., Buttighoffer A., Léorat J., 1999, Proc. 8th SOHO Workshop, Plasma Dynamics and Diagnostics in the Solar Transition Region and Corona. Paris, France, 22–25 June 1999, ESA SP-446

Hu Y.Q., Wu S.T., 1984, J. Comput. Phys. 55, 33

Lau Y.-T., Siregar E., 1996, ApJ 465, 451

Lele S.K., 1992, J. Comput. Phys. 103, 16

Linker J.A., Van Hoven G., 1990, Geophys. Res. Lett. 17, 2281

Marsch E., 1991, In: Schwenn R., Marsch E. (eds.) Physics of the inner heliosphere vol.2, Springer-Verlag, Berlin, p. 159

Malara F., Primavera L., Veltri P., 1996, J. Geophys. Res. 101, 21597

Ofman L., Davila J.M., 1998, J. Geophys. Res. 103, 23677

Pneuman G.W., Kopp R.A., 1971, Solar Phys. 18, 258

Poinsot T.J., Lele S.K., 1993, J. Comput. Phys. 101, 104

Usmanov A.V., Goldstein M.L., Besser B.P., Fritzer J.M., 2000, J. Geophys. Res. 105, 12675

Vanajakshi T.C., Thompson K.W., Black D.C., 1989, J. Comput. Phys. 84, 343

Vasquez B.J., Hollweg J.V., 1998, J. Geophys. Res. 103, 335

Velli M., Grappin R., Mangeney A., 1989, Phys. Rev. Lett. 63, 1807

Velli M., Landi S., Einaudi G., 1997, In: Shadia Rifai Habbal (ed.) Alfven Wave Propagation at X-Points and Shock Wave Formation in the Solar Corona, Robotic Exploration Close to the Sun: Scientific Basis, Marlboro, MA, April 1996, AIP Conference Proceedings vol. 385, AIP, Woodbury, NY. p. 211

Wang A.H., Wu S.T., Suess S.T., Poletto G., 1993, Solar Phys. 147, 55,

Washimi H., Yoshimo Y., Ogino T., 1987, Geophys. Res. Lett. 14, 487